NANO · MICRO small
www.small-journal.com

Creation of Grooved Tissue Engineering Scaffolds from Architectured Multilayer Polymer Composites by a Tuneable One-Step Degradation Process

Muthu Vignesh Vellayappan, Francisco Duarte, Cyrille Sollogoub, Justin Dirrenberger, Alain Guinault, Jessica E. Frith, Helena C. Parkington, Andrey Molotnikov, and Neil R. Cameron**

The surface properties of biomaterials interact directly with biological systems, influencing cellular responses, tissue integration, and biocompatibility. Surface topography plays a critical role in cardiac tissue engineering by affecting electrical conductivity, cardiomyocyte alignment, and contractile function. Current methods for controlling surface properties and topography in cardiac tissue engineering scaffolds are limited, expensive, and lack precision. This study introduces a low-cost, one-step degradation process to create scaffolds with well-defined micro-grooves from multilayered 3D printed poly(lactic acid)/thermoplastic polyurethane composites. The approach provides control over erosion rate and surface morphology, allowing easy tuning of scaffold topographical cues for tissue engineering applications. The findings reported in this study provide a library of easily tuneable scaffold topographical cues. A strong dependence of neonatal rat cardiomyocyte (NRCM) contact guidance with the multilayers' dimension and shape in partially degraded polylactic acid (PLA)/thermoplastic polyurethane (TPU) samples is observed. NRCMs cultured on samples with a layer thickness of 13 ± 2 µm and depth of 4.7 ± 0.2 µm demonstrate the most regular contractions. Hence, the proposed fabrication scheme can be used to produce a new generation of biomaterials with excellent controllability determined by multilayer thickness, printing parameters, and degradation treatment duration.

1. Introduction

Controlling the cell-material interplay is pivotal in tissue engineering.[1] Significant surface properties that influence cell interactions with biomaterials are surface topography, such as surface roughness or the presence of micropores; surface chemical properties such as surface energy; surface charge; the presence of bioactive molecules on the substrate surface; and surface physical properties such as stiffness and wettability.[2] It has been demonstrated that micromorphological features affect the cell's shape while nanomorphology affects the subcellular sensing mechanism.[3a,b] Likewise, the chemical properties of the material surface are also shown to change cell adhesion behavior.[4] Micro-sized topographic features have been found to have a pronounced impact on cellular contact guidance.[5] The impact of different topographies at the cell scale has been explored recently using various architectures such as microgrooves and micro pillars.[6] The cells respond to these

M. V. Vellayappan, F. Duarte, J. E. Frith, A. Molotnikov, N. R. Cameron
Department of Materials Science and Engineering
Monash University
14 Alliance Lane, Clayton, VIC 3800, Australia
E-mail: andrey.molotnikov@rmit.edu.au; neil.cameron@monash.edu

C. Sollogoub, J. Dirrenberger, A. Guinault
PIMM, Arts et Metiers Institute of Technology
CNRS, Cnam
HESAM University
151 boulevard de l'Hopital, Paris 75013, France

The ORCID identification number(s) for the author(s) of this article can be found under https://doi.org/10.1002/smll.202401902

DOI: 10.1002/smll.202401902

J. E. Frith, N. R. Cameron
Australian Research Council Training Centre for Cell and Tissue Engineering Technologies
Monash University
Clayton, VIC 3800, Australia

J. E. Frith
Australian Regenerative Medicine Institute
Monash University
Clayton, VIC 3800, Australia

H. C. Parkington
Department of Physiology
Biomedicine Discovery Institute
Monash University
26, Innovation Walk, Victoria 3800, Australia

A. Molotnikov
RMIT Centre for Additive Manufacturing
School of Engineering
RMIT University
Melbourne, VIC 3000, Australia

cell-scale architectures through morphological changes,[7] migration pattern variation,[8] nuclear reorganization,[9] and cellular differentiation.[10] Microgrooves have also been found to improve the maturation of cardiomyocytes and the reprogramming efficacy of fibroblasts into cardiomyocytes, compared to biochemical cues.[11]

To date, most studies have used lithography to produce patterns and a single material stiffness, which is not representative of the complexity of the ECM. In reality, cells are subjected to different ECM topographies, mechanical and biochemical cues, and environments with multiple soluble factors and interactions between cells. There is evidence that biomaterial stiffness plays a key role in regulating tissue regeneration.[12] When a cell encounters a substrate characterized by a distinct stiffness or rigidity, the organization and tension of its actin filaments and other constituents of the cytoskeleton are remodeled. Importantly, these change mechanotransductive signaling, ultimately guiding changes in cell fate and function. Consequently, it opens up the ability to influence remodeling of the cell's cytoskeleton and resulting cell fate processes, such as migration or differentiation, by employing topographical cues with diverse surface structures, and by using polymers with different stiffnesses. For example, based on the cell-material interplay, the cytoskeleton can be remodeled, and cell migration can be directed.[13] Bade et al., demonstrated the reorganization of actin fibers in fibroblasts in response to the curvature of a biomaterial surface, leading to effects on cell migration and directionality.[14] Curved surfaces were also found to affect the focal adhesion organization, dynamics, nuclear shape, and gene expression of adherent cells.[1b] Cell-scale curvature reorients the cytoskeleton, alters proliferation and ultimately results in whole epithelium elongation.[15] Even though curved surfaces influence the interaction of cells with materials, previous studies have typically focused on single topographic biophysical cues, either a grooved or curved surface topography. Despite the extensive investigations of micro-scale topography on cellular functionality, the effect of grooves in a multi-material setting is less explored.

One promising combination of the multi-materials includes synthetic polymers poly(lactic acid) (PLA) and thermoplastic polyurethane (TPU). PLA is readily available, with properties that can be easily tuned by the choice of the monomer used (D-lactide, L-lactide, D, L-lactide) and polymerization conditions, resulting in polymers with different mechanical properties and degradation profiles.[16] PLA has further attracted interest for many applications in 3D printing since it can be 3D printed with ease with affordable fused deposition modeling (FDM) printers.[17] However, one of the major setbacks of PLA is poor attachment and proliferation of cells to pristine, untreated PLA samples.[18] Hence, there is a demand for a simple, safe, and highly reproducible method to improve PLA's biocompatibility.[19] This can be achieved by altering PLA's surface chemistry and morphology by using a suitable surface modification technique.[20]

There are various surface modification techniques available that would improve the biocompatibility of PLA.[21] Nonetheless, most PLA surface treatment techniques, including coating, photo-grafting entrapment, and chemical conjugation are expensive and laborious.[22] In contrast, sodium hydroxide (NaOH) surface treatment is cost-effective and quick, and the hydrolysis of PLA can be easily performed. Thus, different groups have tested the efficacy of NaOH treatment on PLA. PLA biocompatibility was improved after its treatment with NaOH, due to improved surface hydrophilicity.[23] Similarly, the contact angle and surface roughness of 3D printed PLA were found to increase after NaOH treatment without any negative impact on the bulk mechanical properties.[24]

In this work, an in-depth study of the effect of NaOH etching on the PLA phase in multilayered PLA/TPU scaffolds with varying layer thicknesses was performed to produce a library of grooved scaffold topographies for tissue engineering applications. Overall, the current research adds new insights to previous PLA degradation studies for its potential use as a component in a novel multilayered, architectured PLA/TPU biomaterial for heart tissue engineering applications.

2. Results and Discussion

2.1. Degradation of the PLA Phase in the PLA, TPU, and Multilayered PLA/TPU 3D Printing Filaments

Three different layer systems of 1x, 3x, and 6x PLA/TPU were produced by multilayer coextrusion. To determine the conditions required to produce micro-grooved substrates, the degradation of PLA and the PLA phase in the 6x PLA/TPU filament, which has the smallest polymer layer thickness, was performed in 1 M NaOH. Then, the morphology of 3D printed samples was examined at different sides after degradation to gain insights on the degradation pattern. Finally, a thorough degradation study was performed using 1x, 3x, and 6x samples using a heat-assisted NaOH surface modification technique. The degradation behavior of PLA/TPU filaments in 1 M NaOH at 37 °C was slow, with only a 2.6% weight loss observed after 8 days (data not shown). This weight loss is likely due to the gradual hydrolysis of the PLA phase within the PLA/TPU material. To accelerate the degradation rate, the temperature was increased to 80 °C. After 6 hr, the weight loss percentages were 78.2% for PLA filaments, 23.2% for PLA/TPU, and just 1.2% for TPU filaments (**Figure 1a**). This confirms that NaOH at 80 °C significantly accelerates PLA degradation while having a negligible effect on TPU. The increased PLA chain end mobility above the glass transition temperature of PLA may have resulted in accelerated degradation at 80 °C. It also likely led to an increased hydrolysis reaction rate, resulting in accelerated degradation at higher temperatures. Consequently, the lower molecular weight PLA began breaking down into smaller particles that dissolved in NaOH. This finding aligns with the

N. R. Cameron
School of Engineering
University of Warwick
Coventry CV4 7AL, UK
N. R. Cameron
Nanotechnology and Catalysis Research Centre (NANOCAT)
Universiti Malaya
Kuala Lumpur 50603, Malaysia

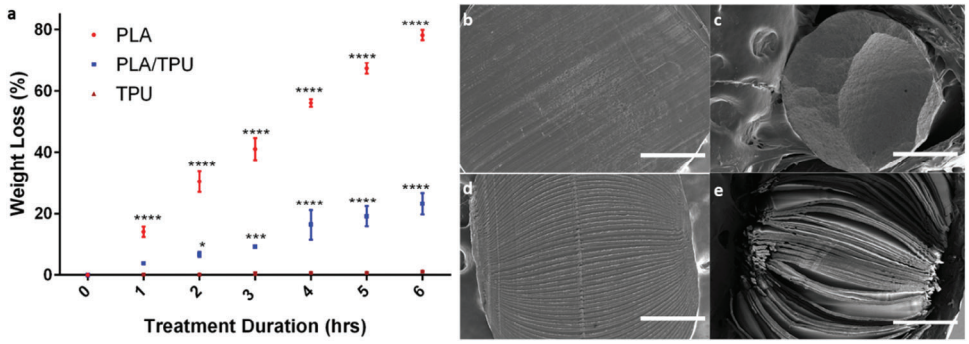

Figure 1. Accelerated degradation of PLA, TPU, and PLA/TPU filaments at 80 °C. a) Weight loss percentage of PLA, TPU, and PLA/TPU filaments at 80 °C. Data are presented as mean ± SD (n = 3) and normalized to control. ($^{*}p < 0.03$, $^{**}p < 0.002$, $^{***}p < 0.0002$, and $^{****}p < 0.0001$ when compared using Two-Way Anova Tukey-Kramer Post-Hoc). SEM images at the cross-section of b) untreated PLA filaments c) 6 h NaOH treated PLA filaments, d) untreated 6x PLA/TPU filaments, and e) 6 h NaOH treated PLA/TPU filaments. Scale bars, 500 µm (b–e).

observed trend in PLA degradation reported by others.[25] It should be noted that TPU is not significantly degraded under these conditions due to its excellent hydrolytic stability, heat resistance, and solvent resistance compared to PLA.[26] Hence, the percentage weight loss in PLA/TPU filament may be attributed to the erosion of PLA layers and not TPU layers (Figure 1a).

SEM was utilized to examine the induced morphological changes in the samples. The PLA filament diameter was reduced from 1.75 to 0.97 ± 0.03 mm in 6 hr, providing further evidence of PLA filament degradation (Figure 1b,c). Initially, the PLA control sample was found to be homogeneous, with few defects (Figure 1b), but after degradation, the filament surface exhibited erosion, resulting in decreased filament diameter and the development of porous zones (Figure 1c). Such erosion is characteristic of polymers undergoing surface erosion.[27] Interestingly, the geometry of the eroded samples was maintained at pH > 13, as water adsorption on the polymer surface helped preserve its shape until the end of the erosion study, which contrasts with bulk erosion behavior.[25b] Furthermore, in PLA/TPU filaments, only the PLA component was found to undergo erosion, supporting the data from the degradation graph with TPU remaining intact (Figure 1a). This observation aligns with the trend in the degradation rate of PLA and TPU, indicating that only PLA degrades under the combined heat and NaOH etching treatment in the PLA/TPU filament (Figure 1b,c). Voids were formed in the eroded PLA/TPU samples, with maximum erosion observed (Figure 1e). After PLA degradation, capillary action may have caused TPU layers to stick together. In this process, chain cleavage occurred rapidly compared with polymer swelling at pH > 13, leading to surface erosion.[25b] Chain cleavage refers to the breaking of the ester functional group on the PLA chain by 1 M NaOH. This process ultimately leads to the degradation of the PLA phase (Figure 1c). This finding is consistent with a previous study that suggests that the accumulation of hydrolysis-induced oligomers within the PLA phase of the scaffold may lead to "autocatalytic degradation". In this process, the free carboxylic acid of the α-chain end units acts as an acid catalyst, leading to the cleavage of the ester bonds in the molecular backbone of the PLA main chains.[25c,d] The PLA and PLA/TPU filament degradation at different time points is shown in Figure S1a–l (Supporting Information).

2.2. Degradation of the PLA Phase in Multilayered 3D Printed Scaffolds

The fabricated multilayered PLA/TPU filaments have layers confined in the cross-section before and after 3D printing. Thus, after 3D printing, the samples were cut to reveal the multilayers. The sectioned portion of the scaffold with multilayers was partially degraded, resulting in micro-sized grooves. Later, the cardiomyocytes were cultured on the grooved multilayered material to study the interaction of cardiomyocytes with the grooved multilayered scaffold. The degradation of 3D printed PLA/TPU structures using 1 M NaOH exhibited polymer-specific behavior (**Figure 2**). The top surface of the structure remained unaffected by the degradation, while the cross-sectional surface of the printed PLA/TPU showed partial degradation. This phenomenon can be attributed to the exposure of PLA exclusively in the cross-section after 3D printing PLA/TPU.[28] Since PLA is present only in the cross-sectional surface and not on the outer surface, it was degraded by NaOH, while TPU, present on both the cross-section and outer surface, remained unaffected. A comprehensive morphological comparison of filaments and 3D printed structures before and after degradation (Figure 2a–p) revealed distinct features. The top surface of PLA/TPU filament showed only cracks after degradation (Figure 2f), whereas the side surface displayed extensive cleavage (Figure 2j) in the center and micro-sized tracks in the cross-sectional surface (Figure 2n). This observation is consistent with the fact that the top surface primarily consists of TPU, while the side surface and cross-section also contain PLA. Notably, PLA is present in the cross-sectional surface of the 3D printed PLA/TPU structure, resulting in the formation of micro-grooves after degradation (Figure 2p), while the top and side surfaces showed limited signs of degradation (Figure 2h,l). The microstructure formed in this process resembled the micro-grooves reported in polydimethylsiloxane substrates.[29]

2.3. Effect of Varying the Infill Angle and Layer Thickness on the PLA Degradation Rate

Varying the infill angle can be beneficial when using 3D printing for tissue engineering scaffolds. It allows more intricate structures to be created, which would be challenging to achieve

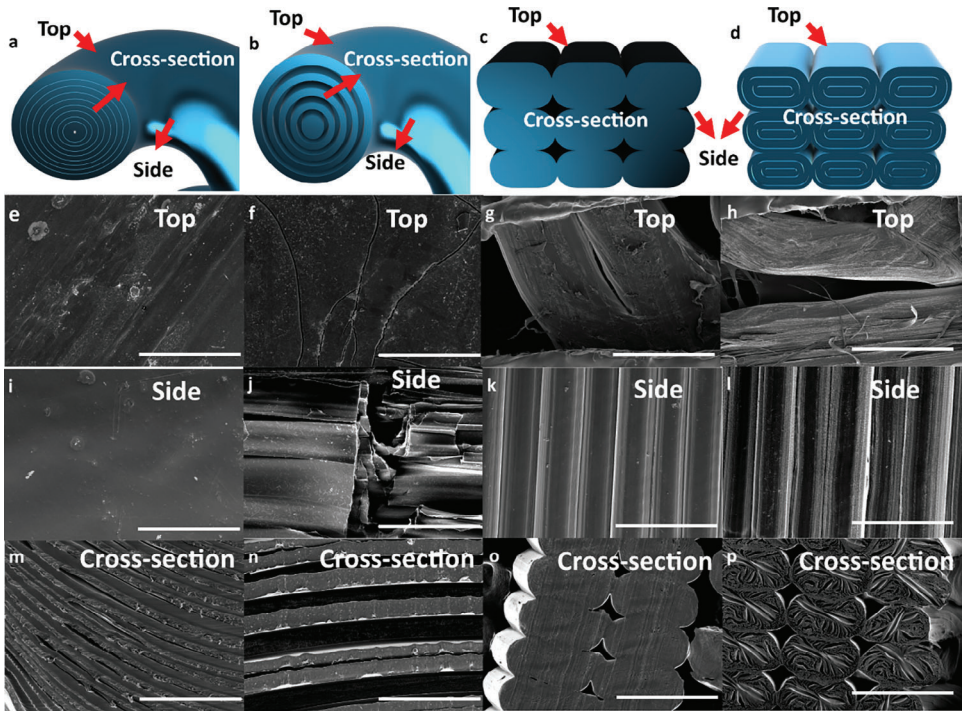

Figure 2. Overall morphological comparison of PLA/TPU before and after degradation. Schematic representation of a) PLA/TPU filament, b) Degraded PLA/TPU filament, c) 3D printed PLA/TPU, d) Degraded 3D printed PLA/TPU. Top surface SEM images of e) PLA/TPU filament, f) Degraded PLA/TPU filament, g) 3D printed PLA/TPU, h) Degraded 3D printed PLA/TPU. Side surface SEM images of i) PLA/TPU filament, j) Degraded PLA/TPU filament, k) 3D printed PLA/TPU, l) Degraded 3D printed PLA/TPU. Cross-sectional surface SEM images of m) PLA/TPU filament, n) Degraded PLA/TPU filament, o) 3D printed PLA/TPU, p) Degraded 3D printed PLA/TPU. Scale bars, 100 µm (e,f,i,j,m,n), 500 µm (g,h,k,l,o,p).

using only one infill pattern. This is especially useful when designing scaffolds for irregular tissue shapes or structures. Additionally, introducing anisotropic properties into the scaffold through varying the infill angle can help better mimic the tissue that it is meant to support. Hence, to achieve varying the infill angle in the presence of grooves, PLA degradation in various 3D printed PLA/TPU structures of different in-fill angles was investigated at various time intervals (Figures S2 and S3, Supporting Information). The comparison of layer thickness and groove depth formation after degradation was demonstrated using SEM and optical profilometry, which played a crucial role in showcasing the formation of grooves in the PLA region using the degradation technique.

Prior to degradation, all three samples exhibited smooth surfaces. After the scaffold was exposed to 1 M NaOH, the PLA region started swelling as shown from inserts of Figure S3 (Supporting Information). The morphology of 3D printed 1x, 3x, and 6x cross-sections at 0°, 90°, and (0 and 90°) infill angle combinations are depicted in Figure S2a–i (Supporting Information). The 0° infill angle resulted in a morphology consisting of straight lines or stripes, while the 90° angle led to a circular or curved morphology (Figure S2c,f,i, Supporting Information). Additionally, noticeable differences in individual polymer layer thickness were observed, with 1x having the largest and 6x having the smallest polymer layer thickness. No distinct variations were observed between the straight and curved layer regions of the samples.

After 4 min degradation (Figure S3a–i, Supporting Information), the PLA layer began to erode in the 3x (Figure S3d–f, Supporting Information) and 6x (Figure S3g–i, Supporting Information) samples. It was evident that degradation in the 0° infill angle structures was less pronounced compared to 90° infill angle PLA/TPU samples, possibly due to a lower exposed PLA surface area in the 0° angle samples. Even in the 0° infill angle 6x samples, surface erosion of PLA was observed. The 6 × 90° infill angle samples exhibited more prominent surface erosion, but the depth appeared shallow, suggesting that the surface erosion of PLA had only just begun. The rate of hydrolytic degradation was likely influenced by the access of water molecules to ester bonds that catalyze the hydrolysis of ester bonds of poly(α-hydroxy acid)s.[30] The microstructure of PLA, influenced by different layer thicknesses in 1x, 3x, and 6x samples, could impact water diffusion leading to the formation of micro-grooves.[31] The 6x sample, with the smallest layer thickness, possibly had the highest diffusion rate, while 1x had the slowest water diffusion.

For samples degraded for 8 min (Figure S4a–i, Supporting Information), surface erosion started to occur in 1x (Figure S4a–c, Supporting Information) and 3x (Figure S4d–f, Supporting Information) samples produced with a 0° infill angle. More significant degradation was observed in the 90° infill angle samples (Figure S4f, Supporting Information). The extent of degradation was highest in the 6x samples, and TPU layers were observed to stick to each other in all 0°, 90°, and (0 and 90°) infill angle combinations. The 1x samples degraded for 12 min showed clear degradation (Figure S5a–c, Supporting Information), with chemical attack producing holes and forming apertures. This demonstrated that

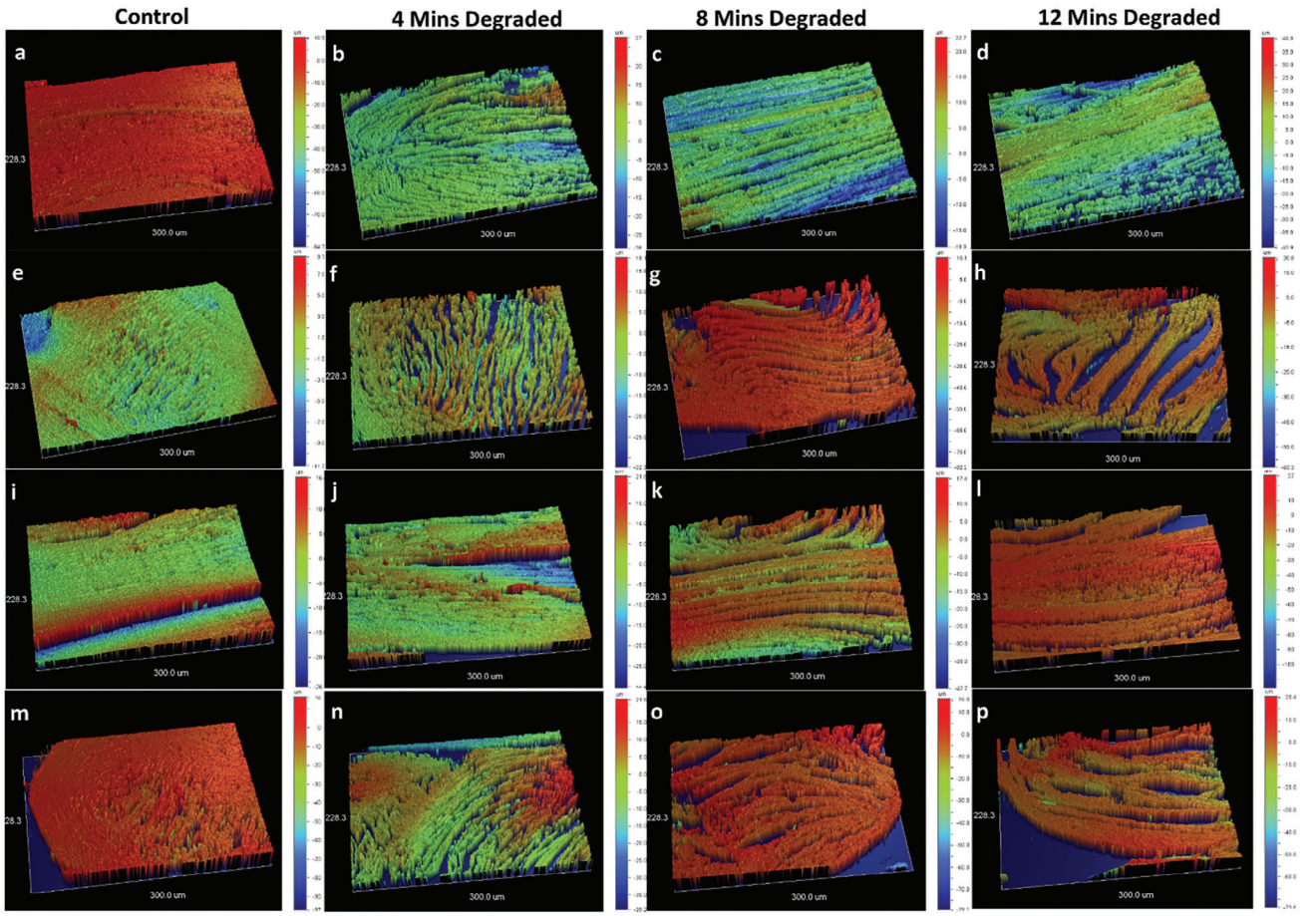

Figure 3. Qualitative groove depth comparison of 3D printed 6x samples using nano-optical profilometry. The columns represent the duration of treatment and the rows represent the infill orientation plus region type (straight vs curved). a–p) represents 0°, 90°, (0 and 90° straight region), and (0 and 90° curved region), respectively.

1x samples with a 0° infill angle required at least 12 min of degradation to obtain a grooved topography (Figure S5a–c, Supporting Information). The groove depth became more visible in the 12-min treated 3x samples (Figure S5d–f, Supporting Information) compared with previous treatment durations. In the 3x sample, there was no sticking of TPU layers, confirming that the surface erosion of PLA had not penetrated deeply. However, this contrasted with the 6x (Figure S5g–i, Supporting Information) samples, where even in the 0° infill angle (Figure S5g, Supporting Information), TPU layers were observed to stick to each other due to capillary action. The lamellar patterns in the 6 × 3D printed samples were more susceptible to selective degradation of PLA than the 1x samples. The thinner PLA layers in the 6x samples may have led to reduced mechanical robustness, causing the structures to collapse onto one another.[20] Consequently, it can be concluded that a 12-min degradation period was too long to maintain the structural integrity of degraded 6x samples.

Given the different rates of PLA erosion for 1x, 3x, and 6x samples, obtaining uniform groove depth among these samples required different degradation time points. Four min was sufficient to produce grooves in all three 0°, 90°, and (0 and 90°) infill angle regions of 6x samples (Figure S3i, Supporting Information). In contrast, 3x samples required at least 8 min of degradation (Figure S4f, Supporting Information), and for 1x samples, a minimum of 12 min of surface degradation was needed to obtain grooved PLA/TPU (Figure S5c, Supporting Information).

2.4. Qualitative and Quantitative Comparison of Groove Depths in 3D Printed PLA/TPU Samples Using Nano-Optical Profilometry

3D Nano-optical profilometer images were acquired to provide information regarding the depth of the eroded PLA surface. A "heat map" was created to depict the groove depth at various points in the multilayered sample (**Figure 3**). Notably, the degradation appears almost identical between the straight regions in the 0° sample (Figure 3a–d) and the straight regions in the (0 and 90°) sample (Figure 3i–l). The same trend is observed for curved regions in the 90° (Figure 3e–h) and (0 and 90°) degrees (Figure 3m–p), regardless of the overall infill angle orientation of the 3D printed sample. Consequently, the qualitative comparison suggests that PLA erosion will be similar in similar regions (either curved-curved or straight-straight) regardless of the infill angle orientation of the 3D printed sample.

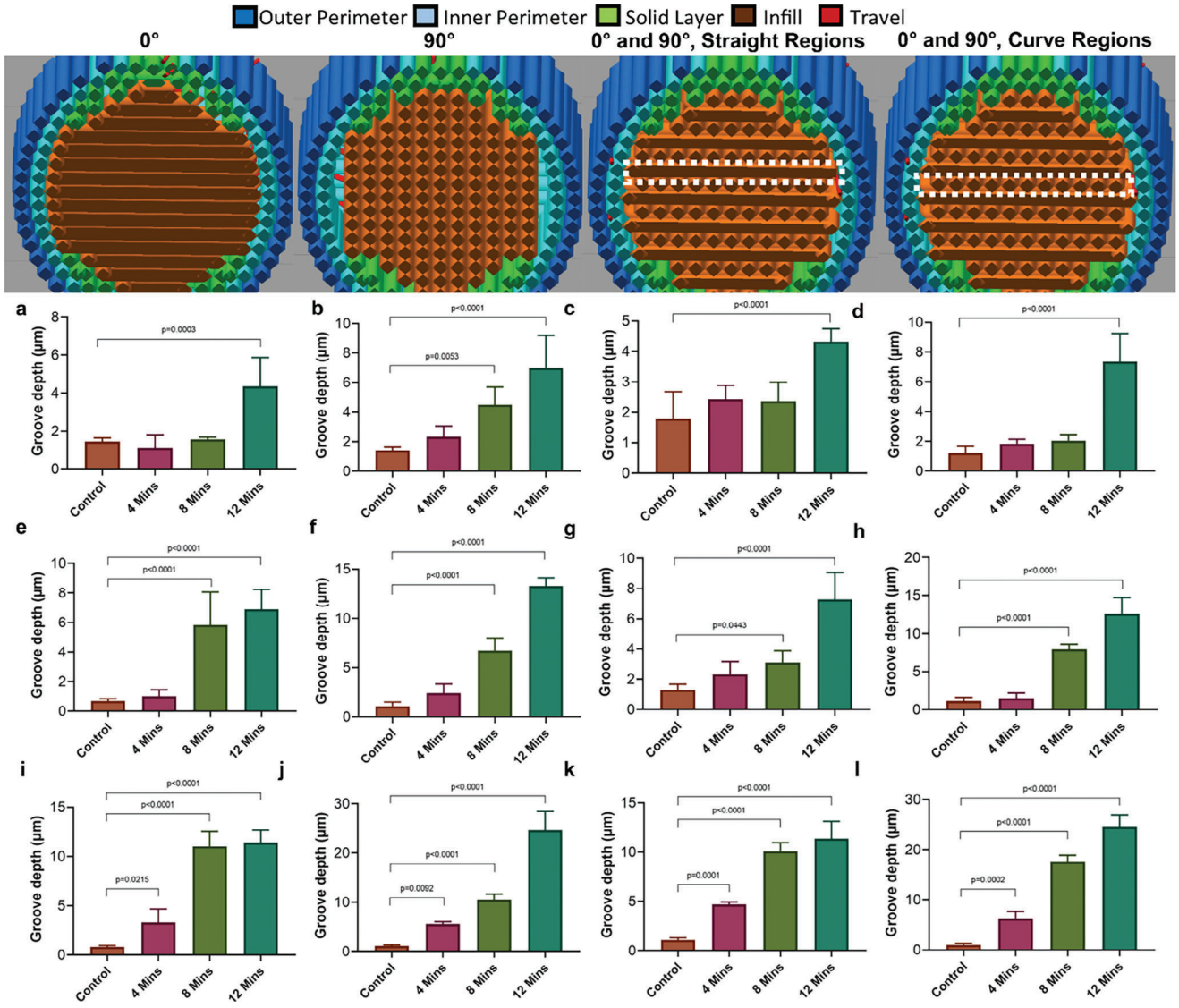

Figure 4. Quantification of PLA/TPU groove depth using nano-optical profilometry measurement before and after degradation. The columns represent the infill orientation plus region type (straight vs curved), and the rows represent the PLA/TPU filament type. a–l) represents 0°, 90°, (0 and 90° straight region), and (0 and 90° curve region), respectively. The second row (a-d) is the groove depths of 1x, the third row (e–h) is the groove depths of 3x and the fourth row (i–l) is 6x samples.

The 6x samples have the lowest individual polymer layer thickness compared with 1x (Figure S6, Supporting Information) and 3x (Figure S7, Supporting Information) samples, as confirmed by profilometer images (Figure 3a–p). Due to the layer thickness being only a few microns, it results in a higher surface area, which drastically accelerates the surface erosion process when exposed to the NaOH solution. Consequently, just 4 min of degradation resulted in noticeable PLA surface erosion. A 12-min treatment appears to be too long for the 6x samples, as the layers of TPU tend to stick to each other due to capillary action (Figure 3d,h,l,p), and attached TPU layers give the impression of increased layer thickness.

The groove depth seemed to increase with the treatment duration based on the SEM images, and this result was further examined using the nano-optical profilometer. The groove depths were quantified and compared for the degraded 1x, 3x, and 6x samples by examining three infill angles (0°, 90°, and (0 and 90°)) as well as both the straight and curved regions of the (0 and 90°) sample. The results indicate that degradation increases with time for all the samples (**Figure** 4a–l). The groove depths for the 1x samples were not significantly different compared with the control samples until the treatment duration reached 12 min (Figure 4a–d). This aligns with the SEM and 3D optical profilometer images, which show an increase in the number of indentations and wells in the PLA region after 12 min of degradation (Figure S6d,h,l,p, Supporting Information). For the 3x samples, significant degradation was observed in the curved regions after 8 min of degradation (Figure S7f,h, Supporting Information). However, in the 6x samples, a significant difference in groove depth was observed in just 4 min of degradation (Figure 4i–l)

due to the thin layer thickness, which corresponds with the qualitative data (Figure 4b,f,j,n). At 12 min of treatment, the surface appeared to have fewer edge features in SEM and 3D profilometer images, which could be due to the sticking of the TPU layers. The highest groove depth values in the 12 min treated 6x samples (Figure 4i–l) suggest that degradation has progressed deep into the PLA surface.

A comparison of groove depths in similar regions of two different samples was made. For example, 1x with a 0° infill angle will have straight regions, while 1x with (0 and 90°) infill angle will have both straight and curved regions. A Student t-test was performed to check if straight regions in both samples, irrespective of the overall infill angle, have a similar degradation profile. This comparison was made for straight regions first in all 1x, 3x, and 6x samples (Figure S8a–i, Supporting Information), followed by a comparison of curved regions (Figure S9a–i, Supporting Information). The results show no significant differences in groove depths between samples. It is also evident that the mean difference in groove depths between samples narrows with increased treatment duration and becomes almost the same in the 12 min degraded samples. This behavior occurs in both straight (Figure S8c,f,i, Supporting Information) and curved regions (Figure S9c,f,i, Supporting Information). This suggests that the polymer degradation rate is uniform inside the polymer matrix. The erosion kinetics are impacted by two key processes: water diffusion into the PLA phase. If water diffusion into the PLA phase is faster than the degradation of PLA bonds, then bulk erosion occurs, as degradation is not confined to the external surface of PLA. However, if the degradation of PLA chemical bonds is faster than the diffusion of water molecules into the PLA phase, hydrolysis of polymer bonds on the surface occurs, preventing bulk erosion.[25b] In this study, the change in surface topography observed in the degraded PLA/TPU sample indicates surface erosion. The increase in treatment duration results in a smoother surface with fewer pronounced edge features, leading to closer mean values of groove depth.[24b]

The degradation rate is slowest for the 1x samples because of their large layer thickness, resulting in a lower groove depth. The 3x samples have a larger groove depth than 1x, and the 6x samples have the largest groove depth. The hydrolysis of polymer bonds on the PLA surface appears to be the predominant mechanism, leading to confined surface erosion in the PLA region, with the highest degradation observed in 6x, followed by 3x, and finally 1x material. This conclusion aligns with the SEM and 3D profilometer images.

The key difference noted in the degradation results was that the 1x samples exhibited little or no surface erosion until the treatment duration reached 12 min (Figure S6a–p, Supporting Information). This could be attributed to the higher individual polymer layer thickness in the 1x samples compared to the 3x and 6x samples. Additionally, the infill angle orientation influences the layer thickness, with curved regions having narrower layers compared with straight regions, which may result in more surface erosion in the curved regions (Figure S6d, Supporting Information) compared with the straight regions (Figure S6l, Supporting Information). Notably, the degradation appears almost identical between the straight regions in the 0° sample (Figure S6a–d, Supporting Information) and the straight regions in the (0 and 90°) sample (Figure S6i–l, Supporting Information). The same trend is observed for curved regions in the 90° (Figure S6e–h, Supporting Information) and (0 and 90°) degrees (Figure S6m–p, Supporting Information), regardless of the overall infill angle orientation of the 3D printed sample. Consequently, the qualitative comparison suggests that PLA erosion will be similar in similar regions (either curved-curved or straight-straight) regardless of the infill angle orientation of the 3D printed sample.

Comparing the overall degradation of the 3x samples (Figure S7a–p, Supporting Information) with the 1x samples (Figure S6a–p, Supporting Information), a similar trend of surface erosion is observed between straight and curved regions. Notably, significant degradation is observed in just 8 min for the 3x samples. The 3D profilometer images clearly depict that the individual polymer layer thickness of 3x samples is almost halved compared to 1x, which corroborates with the initial SEM individual polymer layer thickness analysis. Erosion between the straight regions in the 0° infill (Figure S7a–d, Supporting Information) and the straight regions in the (0 and 90°) infill angle (Figure S7i–l, Supporting Information) is almost the same. Similarly, degradation in curved regions appears similar for the 90° (Figure S7e–h, Supporting Information) and (0 and 90°) infill angles (Figure S7m–p, Supporting Information), irrespective of the sample's overall orientation.

By varying the duration of treatment, it is possible to adjust the depth of grooves in 3D printed multilayered PLA/TPU materials. This means that the extent of degradation can be easily controlled, allowing for customizable groove depths. Deeper grooves can be achieved with longer treatment durations. The proposed one-step degradation approach enables simultaneous control of erosion rates and surface morphologies. For the 1x, 3x, and 6x samples, the ridge feature sizes (individual layer thickness) were 356 ± 158, 103 ± 25, and 13 ± 2 µm, respectively.[28] Since 3–6 microns of depth for cardiac scaffold application are found to be effective, 4, 8, and 12 min NaOH treatment durations were selected for 1x, 3x, and 6x samples for further cell culture experiments.[13b] The depth features (valley feature sizes) for the straight regions at 0 and 90° were 4.3 ± 0.4, 3 ± 0.8, and 4.7 ± 0.2 µm for 1xD, 3xD, and 6xD samples, respectively.

2.5. Chemical Confirmation of PLA-Derived Functional Groups Post-Degradation

Spectroscopy analysis confirmed that PLA was present in the cross-sections of the 1x, 3x, and 6x samples, both before and after degradation, as shown in Figure S10a–d (Supporting Information). It is crucial to ensure that the grooves are not too deep to avoid capillary action and prevent the TPU layers from sticking to each other. Additionally, the spectroscopy analysis confirmed the presence of partially degraded PLA in the scaffolds. The characteristic absorption bands of PLA, namely a distinct and strong peak at 1744 cm^{-1} attributed to C═O stretching, and a slightly weaker yet sharp peak in 1450–1375 cm^{-1} attributed to C—H bending of alkane methylene groups, were clearly evident in the intact 1x, 3x, and 6x samples.[32] Conversely, these peaks

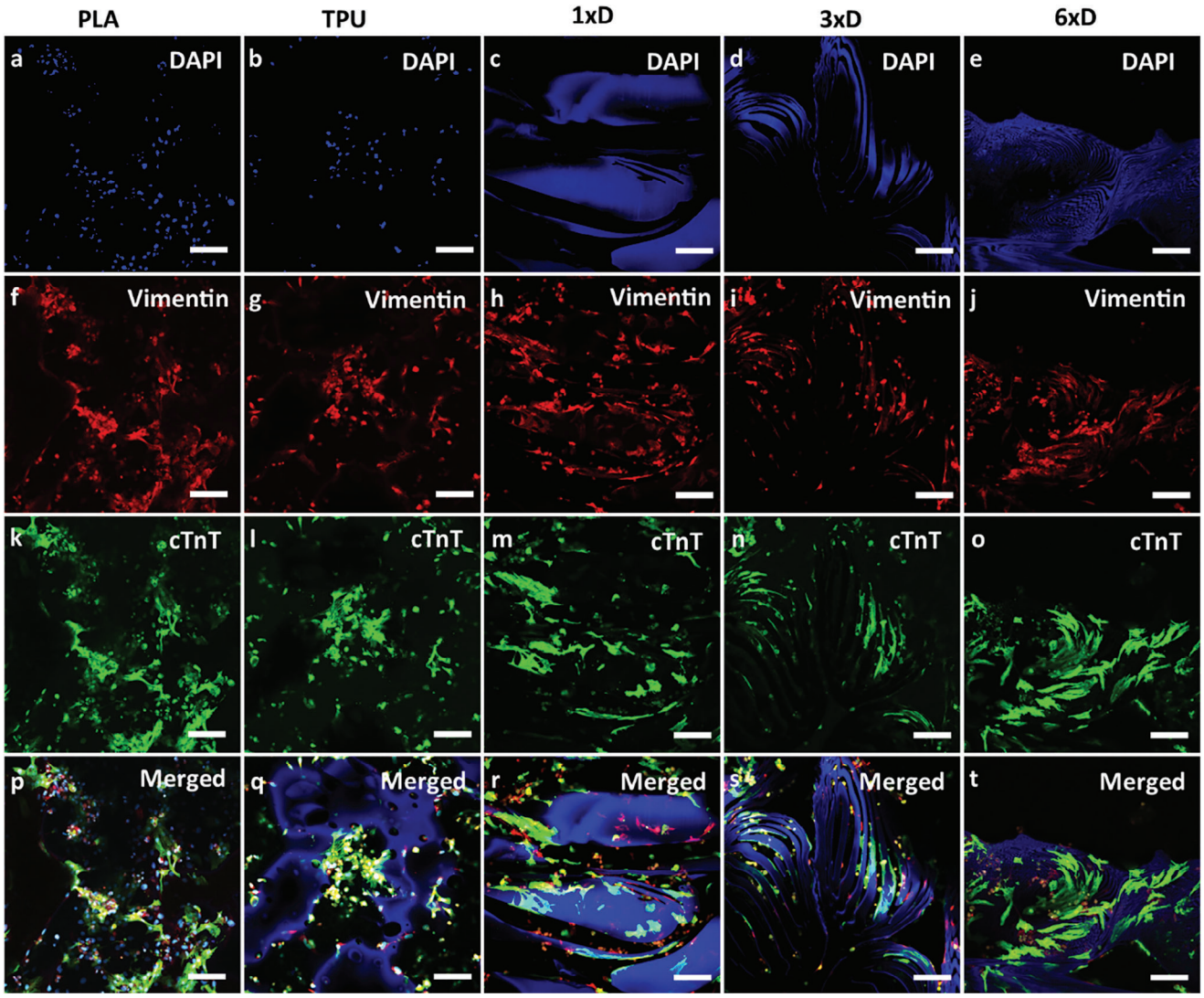

Figure 5. Confocal microscopy images of immunostained NRCM and fibroblast cells on degraded 3D printed scaffolds 3 days after seeding 2.6×10^5 cells cm^{-2}. a,f,k,p) PLA, b,g,l,q) TPU, c,h,m,r) degraded 1x, d,i,n,s) degraded 3x and e,j,o,t) degraded 6x. Red, fibroblasts cytoskeleton (vimentin); green, NRCMs actin filaments (cardiac troponin t); blue, cell nuclei (DAPI) and TPU autofluorescence. Scale bars, 200 µm (a–t).

were not observed in TPU (Figure S10a, Supporting Information). Additionally, the characteristic TPU peak at 3323 cm^{-1}, due to N—H stretching of an aliphatic primary amine, was present in the TPU samples (Figure S10a, Supporting Information).[33] These distinctive observations were consistently noted in both the intact and degraded samples (4, 8, and 12 min) of 1x, 3x, and 6x (Figure S10b,c,d, Supporting Information). Remarkably, this result aligns well with the findings from SEM and optical profilometer analyses, which also demonstrated the presence of PLA even in the 12 min degraded 1x, 3x, and 6x samples.

To conclude, the confirmation of PLA's presence before and after degradation, along with its persistence in the degraded samples, strongly supports the efficacy of the groove formation process in the investigated materials. These results contribute valuable insights to the understanding of the degradation behavior and potential applications of PLA-based 3D printed multilayered materials.

2.6. Comparison of Morphometric Parameters and Function of Neonatal Rat Cardiomyocytes Cultured on Degraded Multilayered Samples

Grooves provide physical cues for cardiomyocytes to align and form functional cardiac tissue,[29a] providing an opportunity for patterned biomaterials to align cells and improve the connectivity and function of cardiac constructs. Therefore, the influence of engineered microscale topographies/grooves on the morphology and function of NRCMs was evaluated. PLA, TPU and straight regions of 0 and 90° infill angles of degraded 1x (1xD) degraded 3x (3xD), and degraded 6x (6xD) samples were used for the analysis (**Figure 5**a–t). Confocal microscopy revealed that neonatal rat cardiac cells (NRCMs plus cardiac fibroblasts) cultured on 1xD with ridge size of 356 ± 158 µm and groove depth of 4.3±0.4 showed minimal induction of alignment or orientation, similar to non-degraded 1x samples.[28] Some cells on degraded 1x

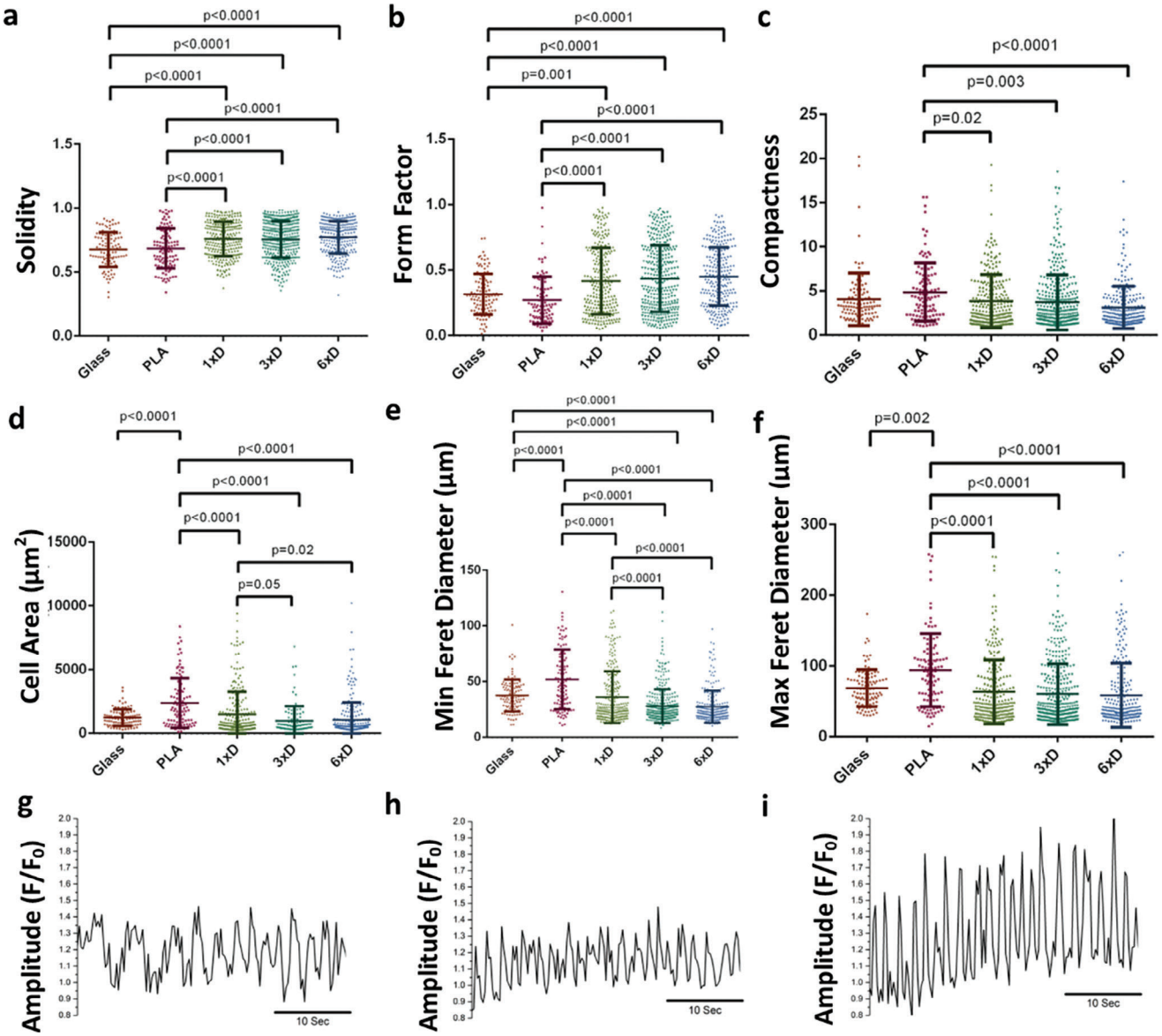

Figure 6. Comparison of morphometric parameters of immunostained NRCMs on control and degraded PLA/TPU samples 3 days after seeding 2.6×10^5 cells cm^{-2}. a) Solidity, b) form factor, c) compactness, d) cell area, e) minimum Feret diameter, and f) maximum Feret diameter. Averaged calcium transients of NRCMs on scaffolds 3 days post-seeding, g) 1xD, h) 3xD, and i) 6xD (n = 3) (scale bar 10 sec). Values expressed as mean ± SEM, (n = 3). One-way ANOVA analysis followed by Tukey multiple comparison test was used for identifying statistical significance.

samples grew in the gaps/grooves, which could be attributed to the larger width of the groove facilitating cell migration or settling (Figure 5h,m,r). However, 3xD samples with a ridge size of 103 ± 25 µm, and groove depth of 3 ± 0.8 µm exhibited noticeable tracking of cells along the walls of the grooves (Figure 5d,i,n,s). In the case of 6xD samples with a ridge size of 13 ± 2 µm, and groove depth of 4.7 ± 0.2 µm, cells appeared to be wider compared to those grown on intact 6x samples, indicating a preference for maintaining original dimensions rather than extending actin filaments.[28]

To evaluate the role of grooves in contact guidance, six NRCM morphometric parameters, namely cell solidity, form factor, compactness, cell area, minimum Feret's diameter, and maximum Feret's diameter, were determined using an established Cell Profiler pipeline (Figure S11, Supporting Information) and compared between 1xD, 3xD, and 6xD samples (**Figure 6**a–f).[28] The highest cell solidity and form factor (Figure 6a,b) were observed for the 6xD samples with layer thickness and depth of 13 ± 2 and 4.7 ± 0.2 µm. These morphometric observations are in agreement with a previous study, where the NRCMs were more spindle-shaped than the pristine PLA and TPU samples, as evidenced by a higher solidity and form factor.[34] Additionally, NRCMs cultured on 6xD had the lowest compactness, demonstrating that they have the least irregular shapes (Figure 6c). The cell area of 6xD was higher than that of the 3xD (layer thickness and depth of 103 ± 25 and 4.7 ± 0.2 µm), demonstrating that the NRCMs

extended their actin filaments to spread on the grooved samples thereby increasing its covered cell area (Figure 6d). The minimum Feret diameter of the NRCMs grown on all the 6xD samples had significantly different values compared to the glass, PLA, and 1xD (layer thickness 356 ± 158 µm, and depth 4.3 ± 0.4 µm) samples possibly resulting from cell spreading across the layers (Figure 6e). However, there was no significant difference between the maximum Feret diameter values of glass, 1xD, 3xD, and 6xD samples (Figure 6f). This result demonstrates that the NRCMs tend to adopt a more elongated shape by having a lower minimum Feret diameter in the 6xD sample, ultimately leading to improved functionality. Thus, the overall result suggests that the measurement values of PLA are very different compared to the 1xD, 3xD, and 6xD samples. The degraded multi-layered samples are quite similar, except for 1xD which has a larger area (albeit still smaller than PLA) and larger min Feret's diameters. Supporting these morphometric findings, the 1xD samples showed randomly distributed contractions, while 3xD and 6xD samples exhibited periods of regularly spaced contractions, with 6xD samples demonstrating the most optimal contractions (Figure 6g–i). This could be attributed to the lateral width of rat NRCMs, almost matching the minimum Feret diameter of degraded 6x.[13b,35]

Synchronous contraction of the cardiomyocytes is crucial to generate the force necessary for the heart to pump blood around the body. Thus, NRCMs contractions were studied and the contraction results were compared to intact multi-layered scaffolds. The NRCMs cultured on 6xD had the most regular contractions, but in intact samples, the 3x sample had the most regular contractions.[28] The 6xD substrate allowed the NRCMs to connect well via gap junctions and contract simultaneously. On the other hand, in other samples, the NRCM cells were not well connected to each other end-to-end, resulting in each cell being independent of its neighbors. The 6xD substrate with a ridge size of 13±2 µm, and groove depth of 4.7±0.2 µm may have resulted in aligned myofibrils along the main cell axis by forming focal adhesions and improving connections between the NRCMs. Further investigation is needed to determine the reason and mechanism for this difference in cell activity. Additionally, the effect of groove topography in a multi-layered material on gene expression during shape changes could also be studied.

Studies have been conducted on the effect of topographical contact guidance using groove width in the range of 200 nm to 20 µm and groove depth of 244 nm to 5 µm. Previous studies show that 13 ± 2 µm groove and ridge width and 4.7 ± 0.2 µm similar to the depth of degraded 6x resulted in the best NRCM morphology and functionality, unlike the remaining degraded 1x and 3x samples grooved samples. These studies have shown that micro-grooves improve cardiomyocyte alignment, elongation, cell connection, and structural organization. Particularly, several studies have reported using a layer thickness of 13 µm and depth of 3 to 5 µm. For example, spin coating was employed on PDMS scaffold, resulting in groove and ridge widths of 20 µm, with a channel depth of 4 µm. This resulted in increased cell alignment and structural organization in hiPSC cardiomyocytes.[36] Similarly, a range of topographic feature sizes was produced using the photolithography method, where groove and ridge widths of 20 µm, with a channel depth of 3 µm, were produced. NRCMs were shown to demonstrate better cell alignment, calcium transient homogeneity, and cell connection.[37] In another study, a photolithographic stereolithographic tandem strategy was utilized to produce groove and ridge widths of 20 µm, with a channel depth of 3 µm topography. Interestingly, an uninterrupted cellular sheet with improved cardiac marker expression was noted in human bone marrow mesenchymal stem cells.[38] Similarly, various studies have reported using groove and ridge widths of 10 µm, with a channel depth of 3 to 4 µm topography.[29c,39] This resulted in improved cellular alignment, sarcomere organization, improved calcium ion cycling properties, and a decrease in cell area in NRCMs.

The success of a biomaterial greatly depends on how well it integrates with the surrounding tissues. The possible mechanism by which partially hydrolyzed PLA improves cell adhesion is linked to submicron roughness created by alkaline hydrolysis of PLA resulting in increased surface hydrophilicity. Partially hydrolyzed PLA may improve the interaction between the cells and the biomaterial at the cell-biomaterial interface by increasing the attachment of focal adhesion proteins. These focal adhesion proteins link the biomaterial and cells' actin cytoskeleton which in turn may activate intracellular focal adhesion signaling pathways, triggering favorable biological responses such as increased cell adhesion and proliferation.[3b]

3. Conclusion

The one-step degradation approach using NaOH treatment of multilayered 3D printed PLA/TPU polymer composites can produce multilayered scaffold materials with microscale grooves for tissue engineering applications. The degraded scaffolds provide an anisotropic surface that results in improved NRCM cell-cell connections and rhythmic contractions. Improved cell-cell communication in the degraded samples could have also contributed to alignment through mechanical cues and signaling pathways. The proposed fabrication method opens up an opportunity to produce differently engineered arrangements of polymeric multimaterials and could facilitate the design and fabrication of novel architectured biomaterials that advance the field of tissue engineering. Future work can explore different materials combinations and the inclusion of additives/functional materials in specific polymer layers. With the advent of multi-nozzle printing systems, further fine-tuning of the scaffold properties will emerge which utilizes combinations of different materials.

4. Experimental Section

Materials: Ingeo Biopolymer 2003D, a polylactic acid (PLA) polymer, was obtained from Nature Works, France, and Elastollan C90A, a thermoplastic polyurethane (TPU) polymer, from BASF, Germany. The PLA polymer exhibited 160 °C melt temperature, 6 g/10 min melt index, 180,000 g mol^{-1} weight average molecular weight, and 1.79 dispersity. Similarly, the TPU polymer exhibited 210 °C melt temperature, 30 to 50 g/10 min melt index, 116,000 g mol^{-1} weight average molecular weight, and 2.3 dispersity. Both the PLA and TPU polymers underwent a drying process under low pressure (104 Pa) at a temperature of 90 °C for 48 h to remove any residual moisture before being utilized in the multilayer co-extrusion process.

3D Printing Filaments Manufactured Using Multilayer Co-Extrusion Process: As described in the earlier work, multilayered PLA/TPU filaments were produced.[28] The PLA and TPU polymer melt was shaped and merged using a feedblock which was then delivered to the flat die in

well-defined polymer stacks. Within the feedback, the PLA and TPU melted and oriented to the A/B/A configuration. Then the layers were multiplied using layer-multiplying elements (LMEs) which work based on Baker's transformation.[40] This transformation involved cutting the melt in half vertically, compressing and re-stretching each half until it regained its original width, effectively increasing the number of layers. The samples were codified according to the number of LMEs used: 1x for one LME, 3x for 3 LMEs, and 6x for 6 LMEs. The number of polymer layers in each is 5, 17, and 129, respectively. A weight composition of 50% PLA and 50% TPU was achieved by using the same method as described in the previous work.[28]

Printability of Fabricated Filaments: The fabricated filaments 1x, 3x, and 6x filaments were 3D printed using Flashforge Creator Pro 2 3D printer with optimized print parameters. Layer height was defined as 320 µm. Percentage infill was set at 100%, and infill angles of 0°, 90°, and (0° and 90°) were used. The nozzle temperature used was set at 220 °C for all prints. The 3D printer platform temperature was 60 °C for all the samples to aid the adhesion of the polymer melt onto the build plate.

Filament Degradation: 6x filament sections 5 mm in length were cut using a sharp carbon steel surgical blade. In the first set of degradation tests, the samples were immersed in 3 ml of 1 M NaOH solution in 5 ml glass vials. The vials were closed and then wrapped tightly using Parafilm to prevent any evaporation. Initially, 37 °C, which was the human body temperature, was used, the vials were agitated at 250 rpm, and the test was carried out for 192 h. The degradation solution was refreshed every day to ensure that the solution pH value remained unchanged during the experiment.

In the second set of experiments, PLA, TPU, and 6x filament sections 5 mm in length were cut and the same protocol, described above, was followed. Instead of mechanical agitation, the samples in glass vials containing 3 ml of 1 M NaOH solution were placed in an oven at 80 °C for 6 h. After washing the samples with distilled water the samples were left to dry overnight, and their weight was measured using a microbalance (Metler Toledo). The sample weight before and after degradation was measured, and percentage weight loss was calculated using the formula (Wa-Wz)/Wa where Wa and Wz represent the control as well as weight after degradation, respectively.[41] Triplicate samples were used for each experiment.

Degradation of 3D Printed Multilayered Architectures—Qualitative Comparison of Groove Depths of 3D Printed Multilayered Architectures: The effect of degradation at 80 °C on the morphology of the filaments and the groove depth of the resulting 3D printed multilayered PLA/TPU architectures produced was studied. Cylindrical shaped scaffolds with 3 mm radius and 3 mm height were 3D printed from 1, 3, and 6x multilayered filaments using a Flash Forge FDM 3D printer. Samples were printed at infill angles of 0°, 90°, and (0° and 90°). After 3D printing, the samples were immersed in a 3 ml vial filled with water at 100 °C to soften the polymer layers. The 3D printed samples were then removed using tweezers and cut at 1.5 mm height using a sharp carbon steel surgical blade to expose the multilayers. Then, the samples were subjected to degradation in 1 M NaOH solution for different treatment durations. The degradation durations used were 4, 8, and capped at 12 min since treatment for more than 12 min resulted in complete degradation of PLA and aggregation of the TPU layers of the 6x samples. Non-degraded samples were kept as controls.

Quantitative Comparison of Groove Depths of 3D Printed Multilayered Architectures: The groove depth after degradation was visualized and quantified using optical profilometry (VeecoWyko NT100) after 10 nm gold sputter coating was applied to enhance the optical reflection of the polymeric samples. Five measurements were taken for each time point, and the results were compared with scanning electron microscopy (SEM) images.

ATR-FTIR Spectroscopy: The attenuated reflectance (ATR) – Fourier transform infrared spectra (FTIR) were recorded for PLA and TPU in PLA, TPU, and PLA/TPU 3D printed articles before and after degradation using Nicolet 6700 ATR-FTIR with 32 sample scans, and resolution 4 cm^{-1} in the spectral range of 4000–500 cm^{-1}. The resultant spectra were baseline-corrected, and the graphs were plotted with OriginPro.

Scanning Electron Microscopy: The cross-section surface of the PLA, TPU, PLA/TPU filaments, and 3D printed structures were observed with FEI NOVA Nano scanning electron microscopy before and after the degradation test. The filament samples were mounted vertically in a suitable cross-section stub while 3D-printed samples were mounted on flat stubs and were iridium-coated using a Cressington 208 HR sputter coater.

Isolation of Neonatal Rat Cardiomyocytes and Calcium Imaging Study: Neonatal rat cardiomyocytes (NRCMs) were isolated from 1-2-day-old Sprague Dawley rat pups. The protocol used[28] was approved by the Monash University Animal Ethics Committee and conforms to the Australian National Health and Medical Research Council code of practice for the use of animals for scientific purposes. Neonatal rat cardiomyocytes (NRCMs) were cultured on degraded 1x PLA/TPU (1x), 3x PLA/TPU (3x), and 6x PLA/TPU (6x) cylindrical scaffolds with a radius of 3 mm and height of 1.5 mm, for 3 days. After 3 days, the scaffolds with the NRCMs were loaded with the calcium indicator Fluo-4 AM (3 µM, Invitrogen, CA, USA) for 15 min at 37 °C and then image acquisition was carried out at room temperature (25 °C), as previously described.[42] 3-day time point was used to observe early morphological changes, cell adhesion patterns, and alignment along the partially degraded grooves. Another reason for choosing the 3-day time frame was that NRCMs have limited time in culture, and shorter durations (such as 3 days) have been used in previous studies due to these reasons.[43] Fluorescence images were captured, responses were corrected for basal fill (F/F_0), and image analysis of the Ca^{2+} signals was performed as described in the previous work.[28]

Qualitative Analysis of NRCM Morphology Upon Exposure to Physical and Chemical Cues: After the Ca^{2+} imaging, the samples with cells still attached were immediately fixed in 4% paraformaldehyde for immunocytochemistry. The cells were washed, permeabilized, blocked, and incubated with primary antibodies overnight at 4°C on a 45 RPM rocker. Immunocytochemistry staining of NRCM (cardiac troponin T–mouse anti-cardiac troponin T antibody, Abcam, ab33589, 1:500 dilution) and fibroblasts (vimentin–rabbit anti-vimentin Abcam ab45939 antibody–cytoskeleton marker, Abcam, 1:500 dilution) was carried out. The following day, the cells were washed four times with Tween buffer for 5 min before incubation in secondary antibodies: mouse Alexa 488, green (1:1000 dilution), and rabbit Alexa 568, red (1:1000 dilution) for 1.5 h at room temperature. After washing once with PBS, the cells were incubated in 4′,6-diamidino-2-phenylindole (DAPI) (1 µL/5 mL PBS) at room temperature for 5 min to stain the nuclei. The cells were washed with PBS three times (5 min each) and mounted in DAKO. The slides were stored at 4 °C overnight before imaging using a Nikon Eclipse confocal microscope, with excitation lasers at 405 nm (blue for DAPI), 488 nm (green for cardiac troponin T), and 561 nm (red for Vimentin) and a 20x oil-immersion objective as reported in the previous work.[28]

Quantification of NRCM Morphometric Parameters Using Image Analysis Software CellProfiler: CellProfiler 4.0.5 was used to measure the dimensions and NCRMs coverage percentage.[44] First, the ND2 images captured with a confocal microscope were converted to separate as reported in the previous work.[28] The effects of the extracellular matrix on the shape of NRCMs were studied in three main groups. The first determined solidity and form factor to establish the protrusive nature of NRCM, while the second group examined compactness to quantify cell elongation. The third group used Feret's diameter and cell area to measure the size of an NRCM on the scaffold. Compactness was the value obtained after dividing the area of the cell by the area of a circle with the same perimeter. Cells that have an elliptical shape will have a lower compactness value. The min and max Feret's diameters were the shortest and longest distances between parallel tangents touching opposite sides of the NRCMs. The NRCM solidity reflects NRCM cell density and was the proportion of pixels in the convex hull. The form factor was calculated as $4 \times \pi \times \text{Area}/\text{Perimeter}^2$.

Statistics: A minimum of three samples were used for each experiment. One-way ANOVA and two-way ANOVA analysis followed by Tukey's multiple comparison tests were used in degradation tests for identifying statistical significance. Similarly, statistical significance was identified for the cell morphometric parameter study by using a two-way Anova analysis followed by Tukey's multiple comparison test. The Student's t-test was used to compare the groove depths between straight regions of 0° versus (0 and 90°). The same test was used to compare degradation in curved regions of 90° versus (0 and 90°). The statistical analysis used Graph Pad Prism 10 software.

Supporting Information

Supporting Information is available from the Wiley Online Library or from the author.

Acknowledgements

The authors thank Monash University for providing the following awards: MGS, MIPRS, and GRITA (received by MVV). The authors thank the ASBTE for presenting the International Lab Travel Award (received by MVV). Special acknowledgments are also due to: MCEM, the Monash Micro Imaging Platform; and the Ramaciotti Centre for Structural Cryo-Electron Microscopy; for providing licenses to use their instruments. NRC acknowledges funding from the ARC for CTET (IC190100026).

Open access publishing facilitated by Monash University, as part of the Wiley - Monash University agreement via the Council of Australian University Librarians.

Conflict of Interest

The authors declare no conflict of interest.

Data Availability Statement

The data that support the findings of this study are available from the corresponding author upon reasonable request.

Keywords

3D printing, biomaterials, multilayer polymers, tuneable degradation

Received: March 10, 2024
Revised: June 3, 2024
Published online:

[1] a) M. P. Sousa, S. G. Caridade, J. F. Mano, *Adv. Healthcare Mater.* **2017**, *6*, 1601462; b) L. Pieuchot, J. Marteau, A. Guignandon, T. Dos Santos, I. Brigaud, P. F. Chauvy, T. Cloatre, A. Ponche, T. Petithory, P. Rougerie, M. Vassaux, J. L. Milan, N. Tusamda Wakhloo, A. Spangenberg, M. Bigerelle, K. Anselme, *Nat. Commun.* **2018**, *9*, 3995; c) C. Morez, M. Noseda, M. A. Paiva, E. Belian, M. D. Schneider, M. M. Stevens, *Biomaterials* **2015**, *70*, 94.

[2] S. Cai, C. Wu, W. Yang, W. Liang, H. Yu, L. Liu, *Nanotechnol. Rev.* **2020**, *9*, 971.

[3] a) A. T. Nguyen, S. R. Sathe, E. K. F. Yim, *J. Phys.: Condens. Mat.* **2016**, *28*, 183001; b) W. Dou, M. Malhi, Q. Zhao, L. Wang, Z. Huang, J. Law, N. Liu, C. A. Simmons, J. T. Maynes, Y. Sun, *Microsyst. Nanoeng.* **2022**, *8*, 26.

[4] a) D. P. Dowling, I. S. Miller, M. Ardhaoui, W. M. Gallagher, *J. Biomater. Appl.* **2011**, *26*, 327; b) A. Carré, V. Lacarrière, *J. Adhes. Sci. Technol.* **2010**, *24*, 815; c) W. L. Kao, H. Y. Chang, K. Y. Lin, Y. W. Lee, J. J. Shyue, *J. Phys. Chem. C* **2018**, *122*, 694.

[5] a) X. F. Walboomers, H. J. Croes, L. A. Ginsel, J. A. Jansen, *Biomaterials* **1998**, *19*, 1861; b) P. Uttayarat, G. K. Toworfe, F. Dietrich, P. I. Lelkes, R. J. Composto, *J. Biomed. Mater. Res., Part A* **2005**, *75*, 668; c) C. J. Bettinger, R. Langer, J. T. Borenstein, *Angew. Chem., Int. Ed.* **2009**, *48*, 5406.

[6] a) J. Carthew, H. H. Abdelmaksoud, K. J. Cowley, M. Hodgson-Garms, R. Elnathan, J. P. Spatz, J. Brugger, H. Thissen, K. J. Simpson, N. H. Voelcker, J. E. Frith, V. J. Cadarso, *Adv. Funct. Mater.* **2022**, *32*, 2100881; b) J. Carthew, J. B. J. Taylor, M. R. Garcia-Cruz, N. Kiaie, N. H. Voelcker, V. J. Cadarso, J. E. Frith, *ACS Appl. Mater. Interf.* **2022**, *14*, 23066.

[7] a) W. Li, Q. Y. Tang, A. D. Jadhav, A. Narang, W. X. Qian, P. Shi, S. W. Pang, *Sci. Rep.* **2015**, *5*, 8644; b) J. L. Charest, M. T. Eliason, A. J. García, W. P. King, *Biomaterials* **2006**, *27*, 2487.

[8] a) K. H. Song, S. J. Park, D. S. Kim, J. Doh, *Biomaterials* **2015**, *51*, 151; b) J. A. Mitchel, D. Hoffman-Kim, *PLoS One* **2011**, *6*, e24316; c) A. Leclerc, D. Tremblay, S. Hadjiantoniou, N. V. Bukoreshtliev, J. L. Rogowski, M. Godin, A. E. Pelling, *Biomaterials* **2013**, *34*, 8097.

[9] L. E. McNamara, R. Burchmore, M. O. Riehle, P. Herzyk, M. J. P. Biggs, C. D. W. Wilkinson, A. S. G. Curtis, M. J. Dalby, *Biomaterials* **2012**, *33*, 2835.

[10] K. Yang, H. Jung, H. R. Lee, J. S. Lee, S. R. Kim, K. Y. Song, E. Cheong, J. Bang, S. G. Im, S. W. Cho, *ACS Nano* **2014**, *8*, 7809.

[11] J. Sia, P. Yu, D. Srivastava, S. Li, *Biomaterials* **2016**, *103*, 1.

[12] a) P. A. Janmey, D. A. Fletcher, C. A. Reinhart-King, *Physiol. Rev.* **2020**, *100*, 695; b) A. Michele, B. Elisabetta, T. M. Grazia, C. Mariano, C. Vanessa, A. Andrea, C. Annamaria, *Cells* **2019**, *8*, 1036.

[13] A. Tijore, S. A. Irvine, U. Sarig, P. Mhaisalkar, V. Baisane, S. Venkatraman, *Biofabrication* **2018**, *10*, 025003.

[14] N. D. Bade, T. Xu, R. D. Kamien, R. K. Assoian, K. J. Stebe, *Biophys. J.* **2018**, *114*, 1467.

[15] P. Rougerie, L. Pieuchot, R. S. dos Santos, J. Marteau, M. Bigerelle, P.-F. Chauvy, M. Farina, K. Anselme, *Sci. Rep.* **2020**, *10*, 14784.

[16] a) M. Spinu, C. Jackson, M. Y. Keating, K. H. Gardner, *J. Macromol. Sci. A* **1996**, *33*, 1497; b) S. Farah, D. G. Anderson, R. Langer, *Adv. Drug Delivery Rev.* **2016**, *107*, 367; c) K. Masutani, Y. Kimura, in *Poly(lactic acid) Science and Technology: Processing, Properties, Additives and Applications*, (Eds: A. Jiménez, M. Peltzer, R. Ruseckaite), The Royal Society of Chemistry, **2014**, ch. 1, pp. 1–36.

[17] a) E. G. Gordeev, E. S. Degtyareva, V. P. Ananikov, *Russ. Chem. Bull.* **2016**, *65*, 1637; b) A. Ambrosi, M. Pumera, *Chem. Soc. Rev.* **2016**, *45*, 2740.

[18] a) R. Rebelo, M. Fernandes, R. Fangueiro, *Procedia Eng.* **2017**, *200*, 236; b) A. Przekora, *Int. J. Mol. Sci.* **2019**, *20*, 435; c) M. Wang, P. Favi, X. Cheng, N. H. Golshan, K. S. Ziemer, M. Keidar, T. J. Webster, *Acta Biomater.* **2016**, *46*, 256.

[19] M. M. S. Mohd Sabee, N. A. Kamalaldin, B. H. Yahaya, Z. A. Abdul Hamid, *J. Polym. Mater.* **2016**, *33*, 191.

[20] C. Cummins, P. Mokarian-Tabari, J. D. Holmes, M. A. Morris, *J. Appl. Polym. Sci.* **2014**, *131*, 40798.

[21] A. A. John, A. P. Subramanian, M. V. Vellayappan, A. Balaji, S. K. Jaganathan, H. Mohandas, T. Paramalinggam, E. Supriyanto, M. Yusof, *RSC Adv.* **2015**, *5*, 39232.

[22] C. Argentati, F. Morena, P. Montanucci, M. Rallini, G. Basta, N. Calabrese, R. Calafiore, M. Cordellini, C. Emiliani, I. Armentano, S. Martino, *Polymers* **2018**, *10*, 140.

[23] K. Zhao, X. Yang, G. Q. Chen, J. C. Chen, *J. Mater. Sci. Mater. Med.* **2002**, *13*, 849.

[24] a) L. R. Jaidev, K. Chatterjee, *Mater. Des.* **2019**, *161*, 44; b) M. Schneider, N. Fritzsche, A. Puciul-Malinowska, A. Baliś, A. Mostafa, I. Bald, S. Zapotoczny, A. Taubert, *Polymers* **2020**, *12*, 1711.

[25] a) M. Hakkarainen, A. C. Albertsson, S. Karlsson, *Polym. Degrad. Stabil.* **1996**, *52*, 283; b) F. Burkersroda, L. Schedl, A. Göpferich, *Biomaterials* **2002**, *23*, 4221. c) M. Elsawy, H. Kim, W. Park, A. Deep, *Renewable Sustainable Energy Rev.* **2017**, *79*, 1346; d) H. Xu, X. Yang, L. Xie, M. Hakkarainen, *Biomacromolecules* **2016**, *17*, 985.

[26] M. Herrera, G. Matuschek, A. Kettrup, *Polym. Degrad. Stabil.* **2002**, *78*, 323.

[27] A. Göpferich, R. Langer, *J. Polym. Sci. Pol. Chem.* **2003**, *31*, 2445.

[28] M. V. Vellayappan, F. Duarte, C. Sollogoub, J. Dirrenberger, A. Guinault, J. E. Frith, H. C. Parkington, A. Molotnikov, N. R. Cameron, *Adv. Funct. Mater.* **2023**, *33*, 2301547.
[29] a) N. E. Oyunbaatar, D. H. Lee, S. J. Patil, E. S. Kim, D. W. Lee, *Sensors* **2016**, *16*, 1258; b) C. Xu, L. Wang, Y. Yu, F. Yin, X. Zhang, L. Jiang, J. Qin, *Biomater. Sci.* **2017**, *5*, 1810; c) C. Rao, T. Prodromakis, L. Kolker, U. A. Chaudhry, T. Trantidou, A. Sridhar, C. Weekes, P. Camelliti, S. E. Harding, A. Darzi, M. H. Yacoub, T. Athanasiou, C. M. Terracciano, *Biomaterials* **2013**, *34*, 2399.
[30] a) D. Cam, S. Hyon, Y. Ikada, *Biomaterials* **1995**, *16*, 833; b) E. W. Fischer, H. J. Sterzel, G. Wegner, *Kolloid Z. Z. Polym.* **1973**, *251*, 980.
[31] P. Feng, J. Jia, M. Liu, S. Peng, Z. Zhao, C. Shuai, *Mater. Des.* **2021**, *210*, 110066.
[32] S. Kamyar, M. Ahmad, W. Yunus, N. Ibrahim, R. Abdul Rahman, M. Jokar, M. Darroudi, *Int. J. Nanomed.* **2010**, *5*, 573.
[33] Y. H. Lee, B. K. Kang, H. D. Kim, H. J. Yoo, J. S. Kim, J. H. Huh, Y. J. Jung, D. J. Lee, *Macromol. Res.* **2009**, *17*, 616.
[34] W. Hawkes, E. Marhuenda, P. Reynolds, C. O'Neill, P. Pandey, D. G. Samuel Wilson, M. Freeley, D. Huang, J. Hu, S. Gondarenko, J. Hone, N. Gadegaard, M. Palma, T. Iskratsch, *Philos. Trans. R. Soc. Lond. B Biol. Sci.* **2022**, *377*, 20220021.
[35] C. Leclech, C. Villard, *Front. Bioeng. Biotechnol.* **2020**, *8*, 551505.
[36] C. F. Yang, Y. H. Hsu, 41st Annual International Conference of the IEEE Engineering in Medicine and Biology Society (EMBC), July **2019**.
[37] C. Zhu, A. E. Rodda, V. X. Truong, Y. Shi, K. Zhou, J. M. Haynes, B. Wang, W. D. Cook, J. S. Forsythe, *ACS Biomater. Sci. Eng.* **2018**, *4*, 2494.
[38] S. Miao, H. Cui, M. Nowicki, S.-j. Lee, J. Almeida, X. Zhou, W. Zhu, X. Yao, F. Masood, M. W. Plesniak, M. Mohiuddin, L. G. Zhang, *Biofabrication* **2018**, *10*, 035007.
[39] a) T. Pong, W. J. Adams, M. A. Bray, A. W. Feinberg, S. P. Sheehy, A. A. Werdich, K. K. Parker, *Exp. Biol. Med.* **2011**, *236*, 366; b) J. Kim, J. Park, K. Na, S. Yang, J. Baek, E. Yoon, S. Choi, S. Lee, K. Chun, J. Park, S. Park, *J. Biomech.* **2008**, *41*, 2396.
[40] A. Bironeau, T. Salez, G. Miquelard-Garnier, C. Sollogoub, *Macromolecules* **2017**, *50*, 4064.
[41] S. Lyu, J. Schley, B. Loy, D. Lind, C. Hobot, R. Sparer, D. Untereker, *Biomacromolecules* **2007**, *8*, 2301.
[42] J. B. Marroquin, H. A. Coleman, M. A. Tonta, K. Zhou, B. Winther-Jensen, J. Fallon, N. W. Duffy, E. Yan, A. A. Abdulwahid, J. J. Jasieniak, J. S. Forsythe, H. C. Parkington, *Adv. Func. Mater.* **2018**, *28*, 1700927.
[43] a) J. Boudreau-Béland, J. E. Duverger, E. Petitjean, A. Maguy, J. Ledoux, P. Comtois, *PLoS One* **2015**, *10*, e0127977; b) K. Bourque, J. Jones-Tabah, D. Pétrin, R. D. Martin, J. C. Tanny, T. E. Hébert, *Sci. Rep.* **2023**, *13*, 12248.
[44] A. E. Carpenter, T. R. Jones, M. R. Lamprecht, C. Clarke, I. H. Kang, O. Friman, D. A. Guertin, J. H. Chang, R. A. Lindquist, J. Moffat, P. Golland, D. M. Sabatini, *Genome Biol.* **2006**, *7*, R100.